

***Ab initio* calculation of the effective Coulomb interactions in MX_2 ($M=\text{Ti, V, Cr, Mn, Fe, Co, Ni}$; $X=\text{S, Se, Te}$): intrinsic magnetic ordering and Mott insulating phase**

A. Karbalaee,¹ S. Belbasi,¹ and H. Hadipour^{2,*}

¹*Department of Physics, Faculty of Science, University of Zanjan, Zanjan 45371-38791, Iran*

²*Department of Physics, University of Guilan, 41335-1914, Rasht, Iran*

(Dated:)

Correlated phenomena such as magnetism and Mott phase are a very controversial issue in two-dimensional transition metal dichalcogenides (TMDCs). With the aim of finding the value of correlation strength and understanding the origin of ferromagnetic order in TMDCs, we first identify relevant low-energy degrees of freedom on both octahedral T and trigonal prismatic H lattices in MX_2 ($M=\text{Ti, V, Cr, Mn, Fe, Co, Ni}$; $X=\text{S, Se, Te}$) and then determine the strength of the effective Coulomb interactions between localized d electrons from the first principles using the constrained random-phase approximation. The on-site Coulomb interaction (Hubbard U) values lie in the range 1.4–3.7 eV (1.1–3.6 eV) and depend on the ground-state electronic structure, d -electron number, and correlated subspace. For most of the TMDCs we obtain $1 < U/W_b < 2$ (the bandwidth W_b), which turn out to be larger than the corresponding values in elementary transition metals. On the basis of the calculated U and exchange J interaction, we have checked the condition to be fulfilled for the formation of the ferromagnetic order by Stoner criterion. The results indicate that experimentally observed MnX_2 ($X=\text{S, Se}$) and VX_2 ($X=\text{S, Se}$) have an intrinsic ferromagnetic behavior in pristine form, although V-based materials are close vicinity to the critical point separating ferromagnetic from paramagnetic phase.

PACS numbers:

I. INTRODUCTION

Electron correlation has been an important issue in low-dimensional systems after the experimental synthesis of graphene^{1,2} and other two-dimensional (2D) materials^{3–5}. Generally 2D materials have less bandwidth than the bulk due to lower continuity of the density of states, as a consequence, strength of the correlation U/W_b , namely the ratio of effective electron-electron interaction U to bandwidth W_b , becomes great⁶. For 2D compounds containing transition metal (TM) atoms, in addition to quantum confinement effects arising from reduced dimensionality, correlation effects are expected to play a crucial role in determining the electronic and magnetic properties due to the presence of narrow t_{2g} or e_g states at the vicinity of Fermi level⁸. One of the consequences of a moderate correlation $U/W_b \sim 1$ or strong correlation $U/W_b \gg 1$ are inducing magnetic ordering^{7,8}, Mott insulator^{8–10}, and etc in low-dimensional systems. For instance, an intrinsic ferromagnetism in the monolayers of TM halides such as CrX_3 ($X=\text{Cl, Br, I}$)^{11–16}, VI_3 ^{17,18}, NiI_2 ¹⁹ has been observed experimentally and confirmed theoretically^{20–24}. Furthermore, due to the large correlation strength $U/W_b > 2$, most of the TM halides exhibit a Mott insulating character especially in the systems with nearly half-filled $3d$ bands⁸. Besides TM halides, other 2D materials such as in $\text{Cr}_2\text{Ge}_2\text{Te}_6$ ⁴, Fe_3GeTe_2 ^{25,26}, VX_2 ($X=\text{Se, Te}$)^{27–32}, TiTe_2 ³³, MnSe_2 ³⁴, CrX_2 ($X=\text{S, Se, Te}$)^{35–41}, CoX_2 ($X=\text{S, Se, Te}$) have been found to show magnetic orderings.

In the mentioned systems, synthesis of the $3d$ TM dichalcogenides (TMDCs) such as MX_2 ($M=\text{V, Cr, Mn}$; $X=\text{S, Se, Te}$) has led to a huge experimental and the-

oretical interest due to the existence of incredibly rich correlated phenomena ranging from room temperature intrinsic ferromagnetism^{5,29–34} to charge density wave ordering^{43–45}, and Mott phase¹⁰. Experimentally, even at room temperature, ferromagnetic order were reported in Mn and V-based MX_2 compounds^{29,34}. The possibility of 100% spin polarization indicates that MX_2 monolayers are promising material for spintronics devices. Also, including the on-site Coulomb interaction leads to Mott insulating behavior for V-based systems due to the presence of a half-filled band¹⁰. However, for most of the $3d$ TMDCs such as CrX_2 , MnX_2 systems and even VX_2 , the origin of the intrinsic ferromagnetism remained controversial and existence of strongly correlated phase is still in doubt^{28,44–49}. In other words, some other opposite studies indicate that the ferromagnetism seen in the TMDCs is extrinsic 2D magnetism stemming from vacancies⁵⁰, or proximity effects^{49,51} which are not able to be precisely eliminated in 2D crystal growth. The formation of such extrinsic magnetic moments and long-range magnetic order induced by atom vacancies in some other 2D nonmagnetic materials such as graphene^{52–55} and MoS_2 ^{56,57} makes absence of intrinsic 2D magnetism for pristine TMDCs more likely. From the theoretical side, magnetic ordering depends strongly on the correlated subspace of the d -shell and its value of electron correlation⁴⁷. Anyway, controversy exists over the intrinsic magnetism in the monolayer of $3d$ TMDCs. Another interesting property of $3d$ TMDCs such as trigonal prismatic phase of CrX_2 and VX_2 is valley polarization^{35,58}. Most of the valleytronic MX_2 have a appropriate spin-polarized bandgap of 1.0 eV and spontaneous valley polarization are found to be about 40–90 meV^{58,59}, large

enough for valleytronic devices. The presence of both large valley polarization and spin splitting in a single material are attractive for the research on valleytronic and spintronic applications.

To prevail over the problems of band gap underestimation in Density functional theory (DFT) based on the local density approximation (LDA) or generalized gradient approximation (GGA) and to improve band dispersion to find proper valley polarization, GWA (in particular self-consistent GW + spin orbit coupling) was performed to induce many-body correction^{45,60–63}. However, due to presence of narrow d bands in TMDCs monolayer, the refined methods such as DFT+ U and DFT plus dynamical mean-field theory (DFT + DMFT) will be needed. DFT + U method has been employed to study the electronic properties of some TMDCs^{64–66}, in which the effective U parameters are usually taken from the values found for other materials including the same transition metal atom. Only a few works have been performed the *abinitio* linear response theory and constraint random phase approximation (cRPA)^{67–69} to calculate Hubbard U for VS₂^{10,70}. Indeed, the results of this approach are not extensive and usually are not consistent with those extracted from experiments. This motivates us to do fully *ab initio* calculation to find effective Coulomb parameters for all 3d TMDCs monolayers. The U parameters obtained from *abinitio* calculations not only provide a fundamental understanding of the correlated phenomena in TMDCs, but these effective interaction can also be used in model Hamiltonians thus increasing the predictive power of model calculations.

In this systematic study we first identify appropriate correlated subspaces by constructing Wannier function and then by employing the cRPA approach within the full-potential linearized augmented-plane-wave (FLAPW) method, we determine the effective on-site Coulomb interaction of the d electrons in MX_2 (M =Ti, V, Cr, Mn, Fe, Co, Ni; X =S, Se, Te) for both H and T phases. We find $1 < U/W_b < 2$ in most 3d- MX_2 , making them moderately correlated materials. In non-magnetic state, among the metallic TMDCs, the correlation strength U/W_b turn out to be 2.7 in T-MnX₂ and 1.8 in H-VX₂ with values much larger than the corresponding values in elementary TMs. Based on U and exchange interaction J values, we discuss the tendency of the electron spins to order ferromagnetically by Stoner criterion. The results indicate that experimentally observed MnX₂ (X =S, Se) and VX₂ (X =S, Se) have an intrinsic ferromagnetic behavior in pristine form. Moreover, V-based materials are close to the edge of paramagnetic to ferromagnetic transition

II. COMPUTATIONAL DETAILS

There are two common types of crystal structures in monolayer of TMDCs, which are trigonal prismatic (H) and octahedral (T) coordination⁷². The side and top

views of the crystal structures of T and H phase of MX_2 systems are presented in Fig. 1(a-d). The difference in crystal field splitting generated by surrounding chalcogen X atoms for two lattice of H- MX_2 and T- MX_2 leads to different correlated subspace and play a key role in expressing the differences in the observed electronic and magnetic properties. So, we first briefly describe the crystal structural of MX_2 in T and H phases. The lattice of T- MX_2 consists of triangular nets of TM atoms so that the X atoms are arranged as octahedra with M atoms in the center (see Fig. 1(f)). In this arrangement, d electrons states splits into three lower-energy orbitals t_{2g} (d_{xy} , d_{xz} , d_{yz}) and two higher-energy orbitals e_g (d_{z^2} , $d_{x^2-y^2}$). Note that the octahedron is tilted with respect to the standard Cartesian coordinate x, y, z system, in such a way that C_4 axes (the axes goes through two opposite vertices of the octahedron) is in the z' direction and two opposite faces of the octahedron are parallel to the layers. As shown in Fig. 2(a) and 2(b), in fact, one of the eight triangles of octahedron is lying on the floor and the z axis is perpendicular to this triangle. In this situation, the linear combination of the local t_{2g} orbitals, namely $d_{x'y'}$, $d_{x'z'}$, $d_{y'z'}$ will be the low energy levels. Using the rotation matrix reported in Fig. 2(c), the singlet d_{z^2} orbital which is oriented perpendicular to the layer, is given by $(d_{x'y'} + d_{x'z'} + d_{y'z'})/\sqrt{3}$. The other t_{2g} orbitals, $(d_{y'z'} - d_{x'y'})/\sqrt{2}$, and $(d_{y'z'} + d_{x'y'} - 2d_{x'z'})/\sqrt{6}$, are corresponding to e_{1g} doublet states. The two $d_{z^2}/d_{x^2-y^2}$ are denoted by high-energy degenerate doublets e_{2g} states. By these notation, the non-spin polarized density of d state for T- VSe_2 are presented in

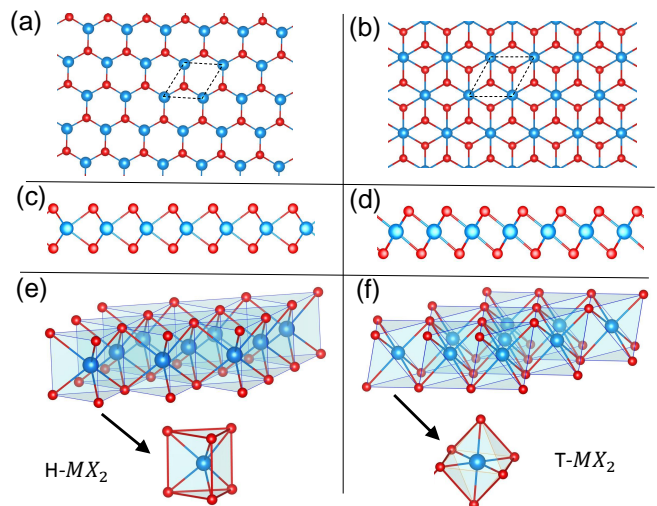


FIG. 1: Top view of the two-dimensional crystal of MX_2 for (a) H phase (b) T phase. Side view of MX_2 for (c) H phase (d) T phase. (e) Trigonal prismatic coordination of one TM and six chalcogen X atoms in H-phase. (f) Octahedral coordination in T phase where in each TM atoms are bound to six X atoms. The blue and red spheres exhibit M and X atoms, respectively

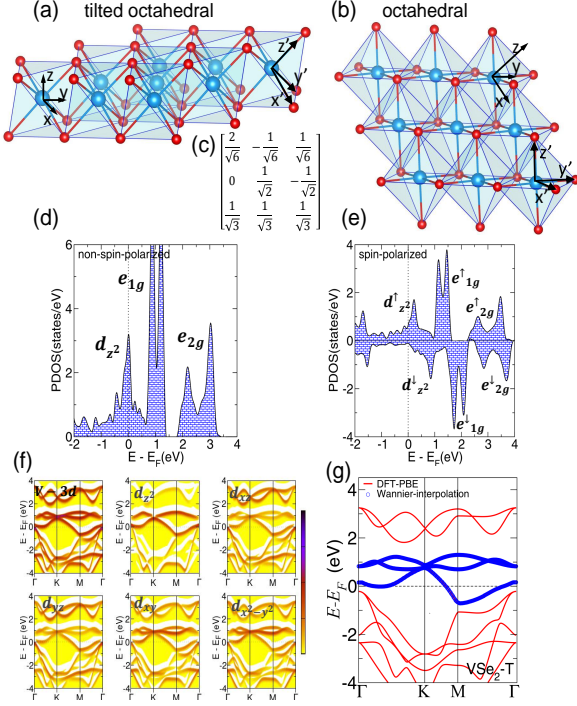


FIG. 2: (a) Tilted octahedral crystal structure with respect to the standard x, y, z Cartesian coordinate in T phase where in two opposite faces of the octahedron are parallel to the layers. (b) The same structure in the rotated state x', y', z' so that it forms a conventional octahedral phase. (c) The rotation matrix which convert x, y, z to x', y', z' coordinate. (d) DOS projected onto $3d$ states of the V atom in the non-spin-polarized calculation for T- VSe_2 . (e) The same as (d) for spin-polarized calculation. (f) The orbital-projected band structures for $3d$ electron of V atom of T- VSe_2 based on DFT-PBE. (g) DFT-PBE (red) and Wannier interpolated band structures (blue) of T- VSe_2 monolayer using $d_{z^2} + e_{g1}$ subspace.

Fig. 2(d). Note that the bands are not of pure d_{z^2} , e_{1g} , and e_{2g} character but are mixtures. Thus, this nominations like d_{z^2} refer to their dominant orbital character.

For H- MX_2 , because of the trigonal prismatic coordination Fig. 1(e), in the crystal-field level, d -shell splits into a singlet d_{z^2} , a low-energy doublet e (d_{xy} and $d_{x^2-y^2}$) and a high-energy doublet e' (d_{xz} , d_{yz}). According to this notation, in Fig. 3(a) we have presented the non-spin polarized density of d state for H-phase of H- VSe_2 .

The basic unit cell is hexagonal in all TMDCs and consists of three atoms. We consider MX_2 (M =Ti, V, Cr, Mn, Fe, Co, Ni; X =S, Se, Te) for both T and H phases. MX_2 unit cells containing one M and two X atoms, are simulated based on the slab model having a 25 \AA vacuum separating them. For the non-spin-polarized as well as for the spin-polarized DFT calculations, the FLAPW method as implemented in the FLEUR code⁷³⁻⁷⁵ is used.

We employ GGA in the Perdew-Burke-Ernzerhof (PBE) parameterization⁷⁶ for the exchange-correlation energy functional. Since, Coulomb matrix elements are

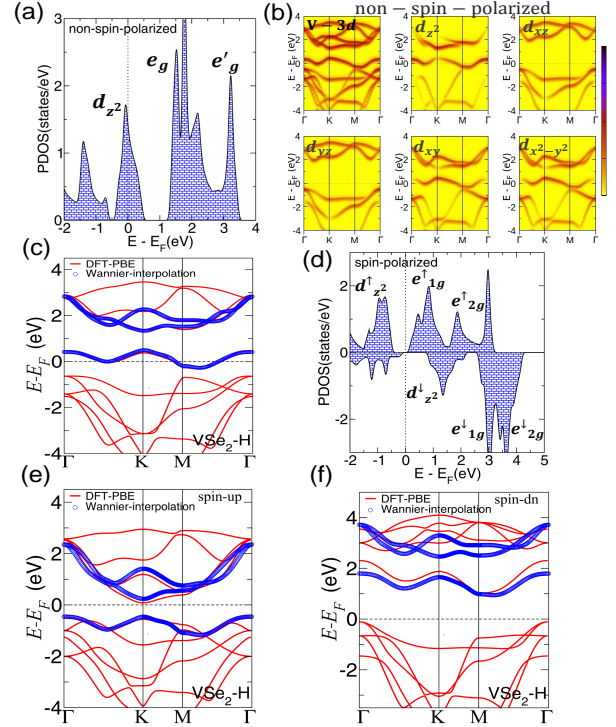


FIG. 3: (a) DOS projected onto $3d$ states of the V atom in the non-spin-polarized calculation for H- VSe_2 . (b) The orbital-projected band structures for $3d$ electron of V atom of H- VSe_2 based on DFT-PBE. (c) DFT-PBE (red) and Wannier interpolated band structures (blue) of H- VSe_2 monolayer using $d_{z^2} + e_g$ subspace. (d) The same as (a) for spin-polarized calculation. DFT-PBE and Wannier interpolated band structures of H- VSe_2 monolayer using $d_{z^2} + e_{g1}$ subspace for (e) spin up and (f) spin down.

almost sensitive to the internal coordinates of the atoms and structural distortions, for all calculations the lattice parameters and atomic positions are chosen to be equal to the optimized parameters with considering the relaxation of the atomic coordinates and possible distortions. The z coordinate of two X atoms are optimized with the residual force less than 0.01 eV/\AA . In the scf calculation, $16 \times 16 \times 1$ k -point grids are used for unit cells of all systems. A linear momentum cutoff of $G_{max} = 4.5 \text{ bohr}^{-1}$ is chosen for the plane waves. The maximally localized Wannier functions (MLWFs)⁷³ are constructed with the Wannier90 library using appropriate bands per M atom. The DFT calculations are used as an input for the SPEX code^{77,78} to determine the strength of Coulomb interaction between correlated electrons from the cRPA and RPA methods^{68,69}. A dense k -point grid $12 \times 12 \times 1$ are used in the cRPA and RPA calculations.

To find strength of screened Coulomb interaction we need to identify correlated subspace which helps to construct Wannier functions properly. So, at first we calculate both non-magnetic and magnetic orbital-resolved density of states (DOS) for all systems which will discussed in next section by details. Here, we have only

presented the orbital projected band structure of VSe₂ in two phases, namely T-VSe₂ and H-VSe₂, in Fig. 2(f) and Fig. 3(b) respectively that resolve the contribution of different d states. The reason why we have chosen VSe₂ case is that the origin of the ferromagnetism and Mott phase in its monolayer limit is still under debate. Also, it was one of the first material in TMDCs, in which ferromagnetism is detected experimentally in monolayer.

As shown in Fig. 2(f) in T phase, in the non-magnetic calculation the mixture of d_{z^2} and e_{1g} ($d_{xy}/d_{x^2-y^2}$) is significant which is also observed in total DOS of d states (see Fig. 2(d)) but t'_{2g} ($d_{z^2} + e_{1g}$) states are well-isolated bands at the vicinity of Fermi level. Although, we construct Wannier functions individually for three d_{z^2} , t'_{2g} , and the full d shell orbitals as a correlated subspace. In t'_{2g} and d cases, the original and the Wannier-interpolated bands agree very well. In Fig 2(g), we have presented a comparison of the non-spin-polarized DFT-PBE band structures with the corresponding Wannier-interpolated bands obtained with the t'_{2g} Wannier orbitals as a minimal subspace for T phase of VSe₂. In other words, it motivates a three-band model for VSe₂ with t'_{2g} Wannier orbitals. In a same way, correlated subspaces are defined for all considered T phase of TMDCs which will be discussed in the next section.

In the H-VSe₂, a single half-filled band which is predominantly d_{z^2} orbital character is well separated from the other bands in the non-magnetic calculation. Thus, to find minimal correlated subspace in the H phase we construct Wannier functions for the d_{z^2} , e_g orbitals. These energy levels are mainly responsible for the electronic, magnetic, and transport properties of H-VSe₂. Note that e'_g states are far from Fermi level and do not contribute to construct half-filled band at E_F . The comparison of the DFT-PBE band structure with Wannier interpolation (see Fig. 3(c)) indicates that the best consistency can be obtained by $d_{z^2} + e_g$ Wannier orbitals as a minimal subspace.

Note that, since one of the aim of this paper is to determine effective Coulomb parameters for low-energy model Hamiltonian of correlated TM materials, the results before symmetry breaking take place, such as non-magnetic U should be calculated. Despite this, we have done spin-polarized calculation for a few systems. As shown in Fig. 2(f) and 3(a), the crystal field splitting is almost small in TMDCs materials. So, considering spin polarization may cause to have problems with entangled bands. It complicates the construction of Wannier function if we use $d_{z^2} + e_g$ subspace in the magnetic calculation. As shown in the Fig. 3(e) and 3(f), the original and the Wannier-interpolated bands do not agree very well. In this case we must go beyond the $d_{z^2} + e_g$ minimal subspace, for instance, full d -shell subspace, which wrongly eliminate a few specific states in the screening.

In the following, we briefly describe cRPA method. The fully screened Coulomb interaction \tilde{U} is related to

the bare Coulomb interaction V by

$$\tilde{U}(\mathbf{r}, \mathbf{r}', \omega) = \int d\mathbf{r}'' \epsilon^{-1}(\mathbf{r}, \mathbf{r}'', \omega) V(\mathbf{r}'', \mathbf{r}'), \quad (1)$$

where $\epsilon(\mathbf{r}, \mathbf{r}'', \omega)$ is the dielectric function. The dielectric function is related to the electron polarizability P by

$$\epsilon(\mathbf{r}, \mathbf{r}', \omega) = \delta(\mathbf{r} - \mathbf{r}') - \int d\mathbf{r}'' V(\mathbf{r}, \mathbf{r}'') P(\mathbf{r}'', \mathbf{r}', \omega), \quad (2)$$

where the RPA polarization function $P(\mathbf{r}'', \mathbf{r}', \omega)$ is given by

$$P(\mathbf{r}, \mathbf{r}', \omega) = \sum_m^{\text{occ}} \sum_{m'}^{\text{unocc}} \varphi_m(\mathbf{r}) \varphi_{m'}^*(\mathbf{r}) \varphi_m^*(\mathbf{r}') \varphi_{m'}(\mathbf{r}') \times \left[\frac{1}{\omega - \Delta_{mm'} + i\eta} - \frac{1}{\omega + \Delta_{mm'} - i\eta} \right]. \quad (3)$$

Here, $\varphi_m(\mathbf{r})$ are the single-particle DFT Kohn-Sham eigenfunctions, and η a positive infinitesimal. $\Delta_{mm'} = \epsilon_{m'} - \epsilon_m$ with the Kohn-Sham eigenvalues ϵ_m . β

In the cRPA approach, in order to exclude the screening due to the correlated subspace, we separate the full polarization function of Eq. (3) into two parts

$$P = P_d + P_r, \quad (4)$$

where P_d includes only the transitions ($m \rightarrow m'$) between the states of the correlated subspace and P_r is the remainder. Then, the frequency-dependent effective Coulomb interaction is given schematically by the matrix equation

$$U(\omega) = [1 - V P_r(\omega)]^{-1} V. \quad (5)$$

It contains, in P_r , screening processes that would not be captured by the correlated subspace and excludes the ones that take place within the subspace.

The matrix elements of the effective Coulomb interaction in the MLWF basis are given by

$$U_{\mathbf{R}n_1, n_3, n_2, n_4}(\omega) = \int \int d\mathbf{r} d\mathbf{r}' w_{n_1 \mathbf{R}}^*(\mathbf{r}) w_{n_3 \mathbf{R}}(\mathbf{r}) U(\mathbf{r}, \mathbf{r}', \omega) w_{n_4 \mathbf{R}}^*(\mathbf{r}') w_{n_2 \mathbf{R}}(\mathbf{r}'), \quad (6)$$

where $w_{n \mathbf{R}}(\mathbf{r})$ is the MLWF at site \mathbf{R} with orbital index n , and the effective Coulomb potential $U(\mathbf{r}, \mathbf{r}', \omega)$ is calculated within the cRPA as described above. We define the average Coulomb matrix elements U , U' , and J in the static limit ($\omega = 0$) as follows? ? :

$$U = \frac{1}{L} \sum_m U_{mm;mm}, \quad (7)$$

$$U' = \frac{1}{L(L-1)} \sum_{m \neq n} U_{mn;mn}, \quad (8)$$

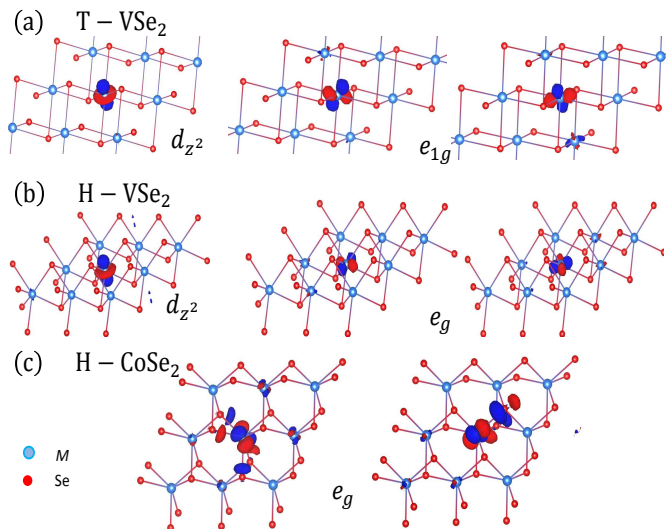


FIG. 4: (a) The d_{z^2} and e_{1g} -like MLWF for V atom of T-VSe₂. (b) The d_{z^2} and e_g -like MLWF for V atom of H-VSe₂. (c) The e_g -like MLWF for Co atom of H-CoSe₂

$$J = \frac{1}{L(L-1)} \sum_{m \neq n} U_{mn;nm}, \quad (9)$$

where L is the number of localized orbitals, i.e., two for e_g and three for t_{2g} orbitals. This parametrization of partially screened Coulomb interactions is the so-called Hubbard-Kanamori parametrization. Similar to the definition of U (U' , J), we can also define the so-called fully screened interaction parameters \tilde{U} (\tilde{U}' , \tilde{J}) as well as unscreened (bare) V . The bare V provides information about the localization of Wannier functions and is a useful parameter in the interpretation of the screened Coulomb interaction parameters.

III. RESULTS AND DISCUSSION

We start with the discussion of appropriate correlated subspace moving from early TiX₂ to late NiX₂ for both T and H phases. To define correlated subspace and also to identify the contribution of different M atoms in the screening, in Fig. 5 we present non-magnetic orbital-resolved DOSs for all considered MX₂ monolayers in T-phase. Similar to V-based system, the comparison of the DFT-PBE band structure with Wannier interpolation shows that for all compounds except Ni-based T-MX₂, the bands with t'_{2g} ($d_{z^2} + e_{1g}$) character is the well-defined correlated subspace. This results is to be expected because of the existence of large t'_{2g} states near the E_F for TiX₂ to CoX₂. In the case of T-NiX₂ systems (see Fig. 5(h) for example), the Fermi level are located in the energy gap between t'_{2g} and e_{2g} bands and the minimal correlated subspace depends on the type of electron or hole doping. The original and the Wannier-interpolated bands do not agree very well when we consider subspace

t'_{2g} . For these systems, we have defined e_{2g} , and full d states as correlated subspace. It means e_{2g} is well-defined subspace in zero-doping, but for optical properties and other correlated phenomenon d subspace would be necessary. As shown in Fig. 5, the orbital-resolved DOS of T-MX₂ with $X = S, Se, Te$ look very similar, thus we have determined Hubbard U parameters identically moving from $X=S$ to Te systems. The Fig. 5 exhibits a strong admixture of chalcogen p with t'_{2g} states which increase as one moves from $M=Ti$ to Ni-based systems and also from $X=S$ to Te ones. To find correlated subspace in these cases, we included a few more states in construction of the Wannier functions. We find U matrix elements of for example p -admixed t'_{2g} states and pure t'_{2g} are nearly identical. However, the delocalization effect arising from admixture of p states will be reflected in the value of coulomb parameters later.

For the H phase of MX₂, the situation for defining the proper subspace is more complicated and differ from one system to another system. The behavior of the electronic structure of $3d$ orbitals across the TM atoms, from $X=S$ to Te, is similar to the case of T-phase. So, we only depicted the orbital resolved DOS only for MSe₂ materials in Fig. 6. For Ti- and V-based MX₂, although single band with predominantly d_{z^2} character is well separated from the other states, but the best consistency are given by $d_{z^2} + e_g$ states. However, because of the great importance of single d_{z^2} band which almost allows defining an effective single band low-energy Hamiltonian, we have also reported the electron-electron interactions for this single band correlated subspace. In $M=Cr-$ to Fe-based MX₂ cases, we see the substantially contribution of both d_{z^2} and e_g states to the DOS around the Fermi energy and, as a consequence, bands with predominantly $d_{z^2} + e_g$ character are obtained to construct Wannier function properly. For the last two series, namely H-CoX₂ and H-NiX₂, we find e_g and e'_g respectively as the minimal correlated subspaces and these layers can be described by a two-orbital effective low-energy model. Although a four-orbital $e_g + e'_g$ low-energy model can be used for the Ni case with caution.

Now, we come to the part we discuss the value of average on-site bare (unscreened) Coulomb interaction V , the average on-site partially (fully) screened interaction parameters U (\tilde{U}), as well as exchange interaction J (\tilde{J}) for correlated subspace electrons of MX₂ systems. The results for T-MX₂ and H-MX₂ are presented in Table I and II respectively. In both H and T phases, bare interaction V increases with increasing the number of electrons in the d -shell. This is to be expected because moving from the left Ti to the right Ni in periodic table, the nuclear charge increases which leads to the contraction of d -wave functions, and subsequently increase the localization of Wannier functions. Note that, the values of V reach a maximum for FeX₂ systems and drop off sharply for CoX₂. For a better understanding, we plot the shape of Wannier orbitals for early VSe₂ and late CoSe₂ systems in Fig. 4. As shown in Fig. 4(c), the

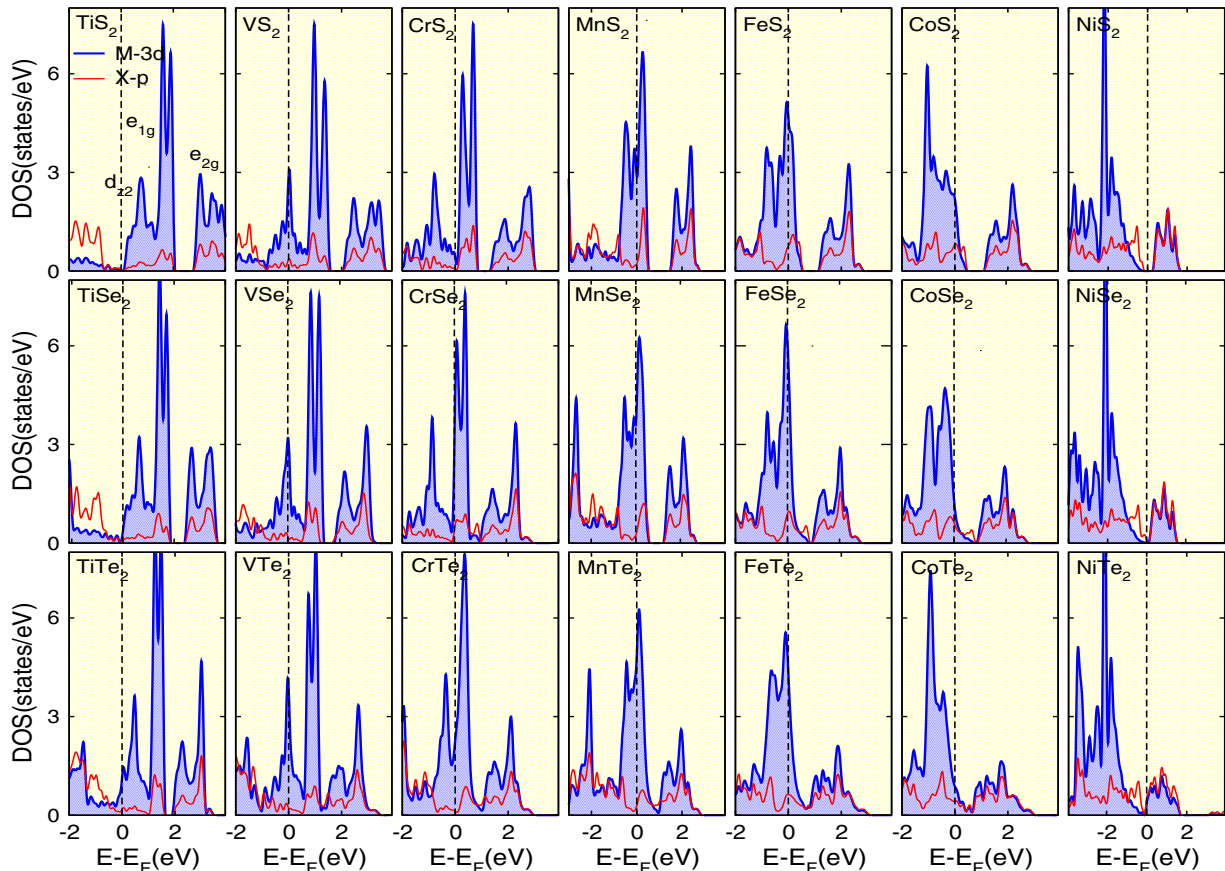


FIG. 5: DOS projected onto $3d$ states of the M atom as well as on p states of the X atoms for T- MX_2 materials. The three distinct peaks of d bands correspond to d_{z^2} , e_{1g} and e_{2g} states.

coupling of e_g states to neighboring chalcogene p states is significant, which leads to a delocalization and, therefore, to smaller V interaction. Furthermore, the results for the chalcogene series MX_2 with $X=S$ to Te shows a reduction in bare V , which is well understood by the increase in the lattice constant, making the Wannier function more extended.

The calculated U values for T- MX_2 (H- MX_2) lie between 1.4 and 3.7 eV (1.1 and 3.6 eV) and depend on the ground-state electronic structure, d -electron number, chalcogene X , and correlated subspace. Since, all screening channels with an excitation energy larger than a few eV around E_F are contributed in cRPA calculations of MX_2 systems, we see strong screening with large difference $V - U$ values in these materials. As seen in Table I and II, the U for M sites tend to increase when M is varied from Ti to Fe. In each chalcogen X and a particular subspace, Hubbard U parameter is determined by two effects: i) Wannier localization effect due to increasing d -electron number and ii) electronic structure effects. Similar to the bare interaction, the first effect is important also in Hubbard U which tend to enhance from Ti to Ni. For the second effect, the insight from orbital-resolved DOS of T-phase (H-phase) depicted in Fig. 5 (Fig. 6) is

that below the d states there is a broad peak of chalcogene p orbitals, which should contribute with $p \rightarrow t'_{2g}$ ($p \rightarrow d_{z^2} + e_g$) transitions substantially to the screening. Indeed, as we move from Ti to Ni, the chalcogen p states gradually move to the lower energy and accompanied by TM $3d$ bands. So, the contribution of $p \rightarrow d$ transition into the polarization function does not change and even slightly reduces when across the series Ti to Fe and give rise to the enhancement of U parameters with increasing $3d$ electron number in both phase of TMDCs. Furthermore, there is another important screening processes via $t'_{2g} \rightarrow e_{2g}$ ($d_{z^2} + e_g \rightarrow e'_g$) in T-phase (H-phase) of MX_2 systems, which only reduce the values of Coulomb parameters and does not change the trend across the TM series.

SchoNhoff et al.⁷⁰ determined Hubbard U values for VS_2 (VSe_2) by employing the cRPA method. The obtained U values are 2.25 eV (2.40 eV), which are smaller than the calculated Coulomb interactions with $d_{z^2} + e_g$ subspace 3.12 eV (2.96 eV) and larger than the Coulomb interactions with d_{z^2} subspace 1.51 eV (1.43 eV) presented in Table II. Using the linear response approach, Isaacs et al. calculated U values for H phase of VS_2 in non-magnetic state and obtained $U = 4.14$ eV¹⁰. This

value is almost 1.0 eV larger than Hubbard interaction in Table II. For the magnetic state, they also determined U interactions for both T and H phases and obtained 3.84 eV for H phase and 3.99 eV for T phase. What subspace to use in construction of the Wannier basis or how to define as the Hubbard U parameter are the possible reasons for this disagreement.

Note that exclusive correlated subspaces must be incorporated into the U calculation, thus, becomes meaningless to compare the Coulomb matrix elements results of H- MX_2 ($M=\text{Ti, V, Co, Ni}$) and T- NiX_2 monolayers with the corresponding results of other MX_2 compounds. For instance, considering the single band d_{z^2} as a correlated subspace for H-phase of VSe_2 , there is an extra sizable screening channels via $d_{z^2} \rightarrow e_g$ transition which can reduce Hubbard U with respect to U for the $d_{z^2} + e_g$ subspace. On the other hand, the value of $U=1.43$ eV for H- VSe_2 is smaller than the $U=1.62$ eV for H- TiSe_2 , which does not follow the increasing trend across the TM series. It can be described by the $M-3d$ and $X-p$ projected DOS around the Fermi energy in Fig. 6. Indeed, as we go from Ti to V in H-phase of MX_2 , the Se-4p states move towards d_{z^2} resulting in more contribution into the polarization function. It compensates the increase in U caused by Wannier localization, leading to the reduction of U interaction with increasing 3d electron number. The same behavior is also observed in S- and Te-based H- MX_2 materials (see Table II).

On going from S to Te within each MX_2 systems, the lattice constant increase, as a consequence, the longer bond lengths lead to smaller orbitals overlap. It can bring the states closer together energetically as shown in Fig. 5 for T phase, and thus smaller energy difference increase the contribution of $p \rightarrow t'_{2g}$ and $t'_{2g} \rightarrow e_{2g}$ transitions ($p \rightarrow d_{z^2} + e_g$ and $d_{z^2} + e_g \rightarrow e'_g$ transition in H- MX_2) into the polarization functions. This means that Coulomb screening is enhanced in the MS_2 - MSe_2 - MTe_2 sequence and thus effective Coulomb interaction U reduce in the same sequence in both T and H phase. The situation for compounds with other correlated subspaces is almost the same. For instance, considering the d_{z^2} correlated subspace the U value is reduced in VTe_2 with respect to the VS_2 case.

In Table I, moving again from Ti to Ni, the same increasing trend is observed for partially inter-orbital Coulomb interactions U' . The obtained J parameters for MX_2 vary in the range 0.24-0.67 eV. Despite the very different range of values in respect to U and U' , exchange J gradually increase with the d -electron number, which are less affected by the electronic structures. In cubic symmetry, Coulomb matrix elements, namely U and U' , and J fulfills the relation $U' = U - 2J$. Even though TMDCs do not have cubic symmetry, this relation is nearly satisfied in most of them.

So far, we focus on the partially screened Coulomb interactions U . To analysis the screening within the correlated subspace, we also calculate fully screened Coulomb interactions \tilde{U} and are reported within parentheses for T-

MX_2 (H- MX_2) in Table I (Table II). Except for the semiconductors T- NiX_2 , H- TiX_2 , and H- CrX_2 , the efficient metallic screening even causes more than 80% difference between U and \tilde{U} parameters. Actually, the calculated \tilde{U} parameters depend strongly on the density of state at the vicinity of E_F . For example, as seen in Table I, the \tilde{U} value for VSe_2 in T-phase (H-phase) is 0.83 eV (0.81 eV) being about 60% smaller than $U=2.14$ eV (2.94) due to the large DOS at E_F and subsequently significant contribution of the $t'_{2g} \rightarrow t'_{2g}$ ($d_{z^2} + e_g \rightarrow d_{z^2} + e_g$) transitions to the polarization function. On the opposite side, in H- TiX_2 , T- NiX_2 , H- CrX_2 , the screening within the correlated subspace is very weak due to the presence of the band gap in the electronic structures, and $(U - \tilde{U})/U$ reaches to 15-25% in these materials. Therefore, the behavior of fully screened interactions \tilde{U} is completely different from U , as they do not follow the ordering with respect to increase of d -electron number.

In the following, we discuss the strength of the electronic correlations, namely the ratio of the effective Coulomb interaction U to the bandwidth W_b (U/W_b) in TMDCs. Note that the U/W_b values are determined for a non-spin-polarized state. Let us start by the results for T phase presented in Table I. For most of the H- MX_2 compounds, we find $1 < U/W_b < 2$ which put these systems in the moderately correlated regime. Therefore, Coulomb interaction play an important role in model Hamiltonian study of the correlation effects in T-phase of TMDCs which induce correlated phenomena like magnetic order. Starting from T- TiX_2 , the correlation strength U/W_b increases and reaches to the maximum in Mn-based TMDCs, and then tends to decrease to Co-based systems. Moreover, electron correlation is strong $U/W_b > 2$ in T- MnX_2 ($X=\text{S, Se}$) materials, as a results, beside magnetic ordering, it becomes unstable to Mott phase.

The U/W_b for the H-phase of TMDCs does not show any clear trend with significant fluctuation around $U/W_b = 1$ from one system to another. We find that in H- MX_2 ($M=\text{Ti, V}$) with d_{z^2} correlated subspace, the correlation strength U/W_b is maximum, bringing them closer to the Mott phase.

It is interesting to compare our calculated U/W_b values with reported ones for elementary TMs and other layered materials containing TM atoms. While, the obtained $1 < U/W_b < 2$ values for TMDC compounds turn out to be larger than the corresponding values in elementary transition metals $U/W_b < 1^6$, they are significantly smaller than the ones calculated for TM-halides $U/W_b > 2^8$. $U/W_b \sim 1$ were found in the case of $M_2\text{C}$ and $M_2\text{CO}_2$ MX-enes, which reveals moderate electronic correlations in these materials⁷. Note that although the *ab initio* Coulomb parameters of TMDCs are smaller than elementary 3d TMs, MX-enes, the narrow bands with d_{z^2} , e_{1g} , and e_g character presented in TMDCs result in a large U/W_b correlation strength.

As seen above, most of the metallic TMDC compounds having almost large correlation strength are expected to

TABLE I: Lattice parameter, orbital type of correlated subspace, bandwidth W_b , on-site intraorbital bare V , intraorbital partially (fully) screened $U(\tilde{U})$, interorbital partially (fully) screened $U'(\tilde{U}')$, partially (fully) screened exchange interaction $J(\tilde{J})$, correlation strength U/W_b , and the DOS at the Fermi level $D(E_F)$ for T- MX_2 compounds.

MX_2	$a(\text{\AA})$	Orbitals	$W_b(\text{eV})$	$V(\text{eV})$	$U(\tilde{U})(\text{eV})$	$U'(\tilde{U}')(\text{eV})$	$J(\tilde{J})(\text{eV})$	U/W_b	$D(E_F)$
TiS ₂	3.4176	$d_{z^2}+e_{1g}$	1.85	15.12	2.22(1.56)	1.41(0.98)	0.40(0.29)	1.20	0.07
TiSe ₂	3.5441	$d_{z^2}+e_{1g}$	1.81	14.69	1.85(1.27)	1.04(0.67)	0.40(0.29)	1.02	0.38
TiTe ₂	3.7409	$d_{z^2}+e_{1g}$	1.98	13.08	1.36(0.96)	0.68(0.49)	0.33(0.22)	0.69	1.15
VS ₂	3.1917	$d_{z^2}+e_{1g}$	2.17	16.25	2.56(0.93)	1.69(0.48)	0.43(0.22)	1.18	3.12
VSe ₂	3.3341	$d_{z^2}+e_{1g}$	1.92	16.09	2.14(0.83)	1.29(0.40)	0.42(0.21)	1.11	3.26
VTe ₂	3.6020	$d_{z^2}+e_{1g}$	2.34	14.47	1.77(0.63)	1.02(0.29)	0.36(0.16)	0.76	4.31
CrS ₂	3.0656	$d_{z^2}+e_{1g}$	2.07	16.68	2.78(1.12)	1.93(0.16)	0.42(0.21)	1.35	0.30
CrSe ₂	3.2243	$d_{z^2}+e_{1g}$	2.16	16.14	2.49(0.60)	1.75(0.12)	0.38(0.17)	1.16	5.80
CrTe ₂	3.6932	$d_{z^2}+e_{1g}$	2.12	15.59	2.27(0.48)	1.52(0.30)	0.37(0.14)	1.07	4.23
MnS ₂	3.3507	$d_{z^2}+e_{1g}$	1.12	18.03	3.02(0.39)	2.06(0.09)	0.49(0.15)	2.70	4.81
MnSe ₂	3.4912	$d_{z^2}+e_{1g}$	1.19	17.71	2.79(0.32)	1.88(0.06)	0.45(0.12)	2.35	5.63
MnTe ₂	3.7448	$d_{z^2}+e_{1g}$	2.38	15.46	2.22(0.30)	1.45(0.07)	0.36(0.11)	0.93	5.92
FeS ₂	3.2013	$d_{z^2}+e_{1g}$	1.51	18.34	3.13(0.60)	2.19(0.37)	0.46(0.11)	2.07	4.13
FeSe ₂	3.3682	$d_{z^2}+e_{1g}$	1.69	17.98	2.81(0.56)	1.86(0.32)	0.46(0.12)	1.66	4.59
FeTe ₂	3.6269	$d_{z^2}+e_{1g}$	2.55	12.80	1.63(0.44)	1.07(0.26)	0.29(0.08)	0.64	3.61
CoS ₂	3.2281	$d_{z^2}+e_{1g}$	1.54	13.19	2.06(1.02)	1.58(0.50)	0.42(0.25)	1.34	2.20
CoSe ₂	3.3704	$d_{z^2}+e_{1g}$	2.63	12.13	1.93(0.74)	1.50(0.40)	0.30(0.15)	0.73	1.31
CoTe ₂	3.6227	$d_{z^2}+e_{1g}$	2.72	10.58	1.57(0.59)	1.06(0.32)	0.24(0.12)	0.58	0.98
NiS ₂	3.3583	e_{2g}	1.75	18.23	3.05(2.30)	2.06(1.56)	0.48(0.38)	1.74	0.00
		d	3.58	21.46	3.67(2.62)	2.41(1.33)	0.63(0.54)	1.02	0.00
NiSe ₂	3.5492	e_{2g}	1.86	18.01	2.16(1.80)	1.02(0.82)	0.58(0.48)	1.16	0.00
		d	3.49	20.28	3.09(2.39)	1.97(1.06)	0.61(0.50)	0.88	0.00
NiTe ₂	3.7806	e_{2g}	2.13	17.65	1.88(1.42)	0.97(0.71)	0.45(0.35)	0.88	0.00
		d	4.32	18.45	2.65(1.87)	1.62(0.92)	0.53(0.41)	0.61	0.00

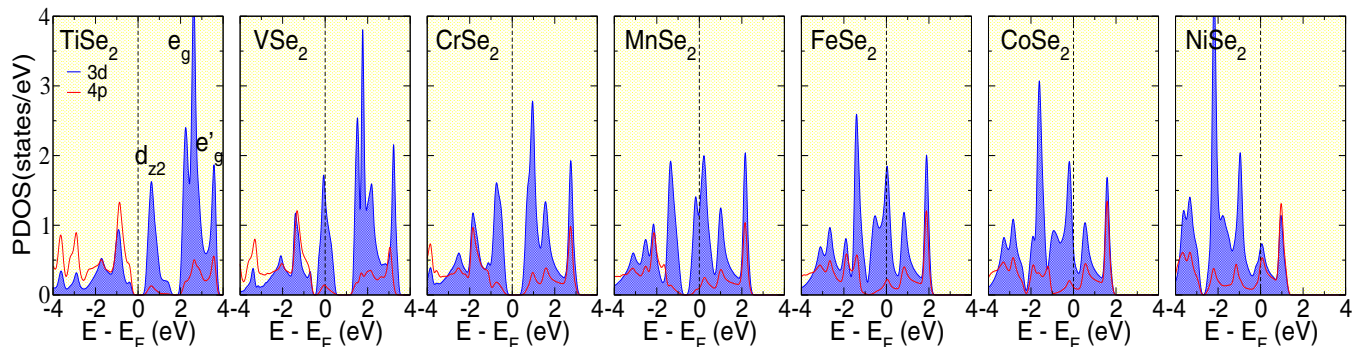


FIG. 6: DOS projected onto 3d states of the M atom as well as on p states of the Se atoms for H- MSe_2 materials. The three distinct peaks of d bands correspond to d_{z^2} , e_g and e'_g states.

display correlation phenomena, such as ferromagnetic ordering. So, in the following, we discuss the appearance of ferromagnetism in these materials. Note that ignoring semiconductors T-NiX₂, H-TiX₂, and H-CrX₂, the correlated subspace of all compounds are partially filled in the non-spin-polarized calculation, thus the Stoner model is well suited to explain the origin of the ferromagnetism of metallic TMDCs. Based on this model, the instability of the paramagnetic state towards ferromagnetic ordering is given by the Stoner criterion $I \cdot D(E_F) > 1$, where I is the Stoner parameter and $D(E_F)$ is the DOS at the Fermi energy in the nonmagnetic state. Solving the multiorbital

Hubbard model, Stollhoff et al. found that relationship between the Stoner parameter I , Hubbard U , and exchange J is given by $I = 3(U + 6J)/25$ ⁷⁹. On the basis of the calculated effective Coulomb parameters U and J presented in Table I and Table II, the Stoner criterion $I \cdot D(E_F) > 1$ for all compounds are presented in Fig. 7. Among the metallic MX_2 , only H-NiX₂ ($X=S, Se, Te$), T-TiX₂ ($X=S, Se, Te$), CrS₂, and CoX₂ ($X=Se, Te$) do not satisfy the Stoner criterion. Almost all theoretically predicted ferromagnetic TMDCs fulfill the Stoner criterion, which is reasonably consistent with our results of spin-polarized total energy calculations and the sizable

TABLE II: The same as Table I for H phase of MX_2 .

MX_2	$a(\text{\AA})$	Orbitals	$W_b(\text{eV})$	$V(\text{eV})$	$U(\tilde{U})(\text{eV})$	$U'(\tilde{U}')(\text{eV})$	$J(\tilde{J})(\text{eV})$	U/W_b	$D(E_F)$
TiS ₂	3.3376	$d_{z^2}+e_g$	2.23	14.47	2.88(2.62)	2.02(1.74)	0.52(0.41)	1.29	0.00
		d_{z^2}	1.20	13.92	1.83	—	—	1.53	0.00
TiSe ₂	3.4739	$d_{z^2}+e_g$	2.39	14.18	2.55(2.26)	1.70(1.32)	0.51(0.39)	1.07	0.00
		d_{z^2}	1.05	13.26	1.62	—	—	1.54	0.00
TiTe ₂	3.7277	$d_{z^2}+e_g$	2.78	13.43	2.03(1.59)	1.25(0.88)	0.47(0.36)	0.73	0.00
		d_{z^2}	0.96	13.09	1.27	—	—	1.32	0.00
VS ₂	3.1650	$d_{z^2}+e_g$	2.97	15.05	3.12(1.16)	2.23(0.59)	0.55(0.34)	1.05	1.52
		d_{z^2}	0.95	14.49	1.51	—	—	1.59	0.65
VSe ₂	3.3066	$d_{z^2}+e_g$	3.02	14.73	2.94(0.81)	2.01(0.33)	0.53(0.31)	0.97	1.80
		d_{z^2}	0.76	14.24	1.43	—	—	1.88	0.62
VTe ₂	3.5458	$d_{z^2}+e_g$	3.40	14.05	2.45(0.65)	1.40(0.25)	0.49(0.29)	0.72	1.72
		d_{z^2}	0.69	13.40	1.12	—	—	1.62	0.51
CrS ₂	3.0552	$d_{z^2}+e_g$	3.41	15.53	3.18(1.96)	2.28(1.43)	0.56(0.34)	0.93	0.00
CrSe ₂	3.2108	$d_{z^2}+e_g$	3.62	15.31	2.93(1.67)	2.01(1.15)	0.53(0.33)	0.81	0.00
CrTe ₂	3.4319	$d_{z^2}+e_g$	3.90	14.49	2.36(1.21)	1.55(0.88)	0.52(0.33)	0.61	0.00
MnS ₂	3.0944	$d_{z^2}+e_g$	3.09	17.11	3.46(0.82)	2.42(0.50)	0.62(0.26)	1.12	1.78
MnSe ₂	3.2335	$d_{z^2}+e_g$	3.32	16.92	3.10(0.68)	2.08(0.42)	0.61(0.24)	0.93	1.65
MnTe ₂	3.5164	$d_{z^2}+e_g$	3.68	16.32	2.68(0.53)	1.79(0.32)	0.58(0.23)	0.73	2.05
FeS ₂	3.1426	$d_{z^2}+e_g$	3.13	18.59	3.58(1.14)	2.45(0.67)	0.67(0.25)	1.14	1.75
FeSe ₂	3.3040	$d_{z^2}+e_g$	3.18	18.46	3.31(1.06)	2.19(0.62)	0.67(0.24)	1.04	1.94
FeTe ₂	3.5238	$d_{z^2}+e_g$	3.29	17.68	2.74(0.95)	1.76(0.54)	0.61(0.22)	0.83	1.81
CoS ₂	3.2037	e_g	2.45	13.40	1.88(0.67)	1.40(0.44)	0.44(0.29)	0.77	2.07
CoSe ₂	3.3406	e_g	2.51	12.93	1.72(0.61)	1.26(0.38)	0.43(0.28)	0.68	1.96
CoTe ₂	3.5485	e_g	2.73	11.50	1.59(0.53)	1.11(0.36)	0.43(0.28)	0.58	2.18
NiS ₂	3.4782	$e_g+e'_g$	2.96	16.99	3.07(0.99)	2.36(0.75)	0.45(0.32)	1.04	0.74
		e'_g	1.31	16.23	1.92(0.75)	1.24(0.62)	0.45(0.31)	1.47	0.42
NiSe ₂	3.4263	$e_g+e'_g$	3.15	15.17	2.61(0.82)	1.94(0.63)	0.39(0.31)	0.83	0.67
		e'_g	1.43	14.38	1.66(0.57)	0.92(0.49)	0.37(0.27)	1.16	0.39
NiTe ₂	3.6122	$e_g+e'_g$	3.23	13.22	1.91(0.62)	1.40(0.47)	0.36(0.27)	0.59	0.69
		e'_g	1.60	12.81	1.17(0.41)	0.55(0.28)	0.35(0.26)	0.73	0.37

magnetic moments presented in right panels of Fig. 7. Note that simple Stoner model does not predict correctly the ground state magnetic phase of H-Co X_2 (X =S, Se, Te) and T-CoS₂. Despite the value of $I.D(E_F)$ for these materials are larger than 1, they have a non-magnetic ground state.

H-VSe₂ and T-MnS₂ were among the first TMDCs materials in which room temperature ferromagnetism were detected experimentally in the monolayer limit. Despite this, a few works indicated that the ferromagnetism observe in the TMDCs is not intrinsic and stem from defects or proximity effects^{49–51}. Also, controversy exists over the Mott insulating behavior in the monolayer of 3d TMDCs. From the theoretical side, the electronic and magnetic ground state depend strongly on taking the correct Hubbard U parameter of the d electrons into account in model Hamiltonian or first-principle calculation. As shown in Fig. 7, in the case of T-MnS₂, the criterion $I.D(E_F) > 1$ is easily satisfied that explains why relatively strong ferromagnetic order is observed in the experiment. Also, it's correlation strength $U/W_b=2.7$ reinforces this idea that the preferred magnetic order is ferromagnetic. The situation in the case of H phase of VSe₂ is not straightforward. We find $I.D(E_F) \sim 1$ which puts system close to the edge of paramagnetic to ferromagnetic transition

(see left panels of Fig. 7). It may explain why there is no agreement in the magnetic phase of VX₂ materials.

IV. CONCLUSION

We have systematically determined the correlated subspaces and effective on-site and interorbital Coulomb interactions between localized electrons in 3d MX_2 (M =Ti, V, Cr, Mn, Fe, Co, Ni and X =S, Se and Te) by employing first *ab initio* calculations in conjunction with a parameter-free cRPA scheme. These Coulomb interactions not only provide a fundamental understanding of the correlated phenomena such as magnetic ordering, charge density wave, or Mott phase in TMDCs, but these effective cRPA parameters can also be used in model Hamiltonians thus increasing the predictive power of model calculations. Based on Hubbard U , exchange interactions J , and electronic structure, we find that for most of the TMDC compounds the correlation strength U/W_b are large enough to be able to put them in moderate and even strong correlated regime. Among TMDC materials, the maximum value $U/W_b=2.7$ eV is obtained in MnS₂ which is almost three time larger than the corresponding value in elementary Mn. We thus expect

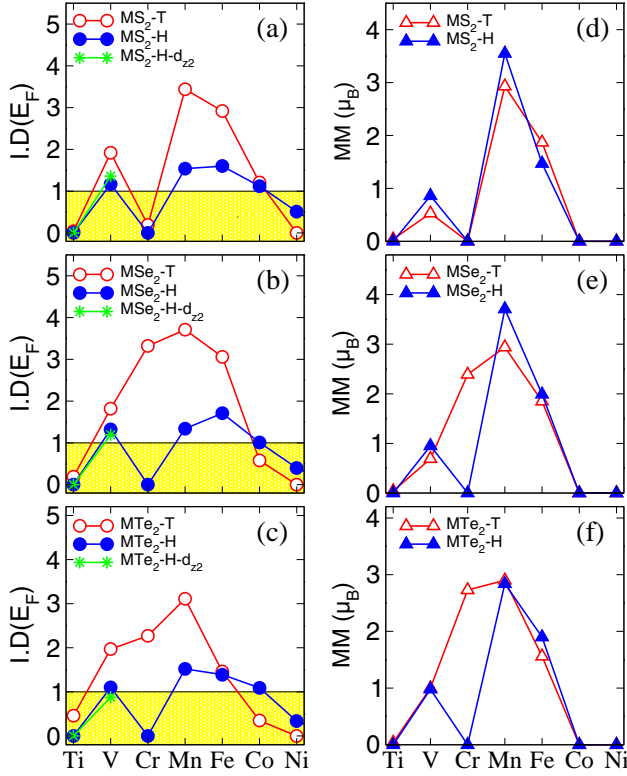


FIG. 7: Stoner criterion for both T and H phase of (a) MS_2 , (b) MSe_2 , and (c) MTe_2 . Calculated magnetic moments (in units of μ_B) of TM atoms for (d) MS_2 , (e) MSe_2 , and (f) MTe_2 . We have also presented the values in the case of d_{z^2} correlated subspace with green star points in H-phase.

electron correlations play an important role in model Hamiltonian studies of the $3d$ -TMDC. Since, there is no agreement on the magnetic ordering of these materials, in particular experimentally observed systems like VSe_2 and MnS_2 , we have checked the condition to be fulfilled for the formation of ferromagnetic order by Stoner criterion $I.D(E_F) > 1$. The results indicate that both MnX_2 ($X=S, Se$) and VX_2 ($X=S, Se$) have an intrinsic ferromagnetic behavior in pristine form, with difference that V-based materials are close vicinity to the critical point separating ferromagnetic from paramagnetic phase

Acknowledgements

.....

* Electronic address: hanifhadipour@gmail.com

¹ A. K. Geim and K. S. Novoselov, Nat. Mater. **6**, 183 (2007).

² M. I. Katsnelson, Mater. Today **10**, 20 (2007).

³ B. Huang, G. Clark, E. Navarro-Moratalla, D. R. Klein, R. Cheng, K. L. Seyler, D. Zhong, E. Schmidgall, M. A. McGuire, D. H. Cobden, W. Yao, Di Xiao, P. Jarillo-Herrero, and X. Xu, Nature (London) **546**, 270 (2017).

⁴ Ch. Gong, L. Li, Zh. Li, H. Ji, A. Stern, Y. Xia, T. Cao, W. Z. Q. Qiu, R. J. Cava, S. G. Louie, J. Xia, and X. Zhang, Nature (London) **546**, 265 (2017).

⁵ W. Yu, J. Li, TS. Herng, et al., Adv Mater. **31**, 40, 1903779 (2019).

⁶ E. Sasoglu, C. Friedrich, and S. Blugel, Phys. Rev. B **83**, 121101(R) (2011); Phys. Rev. Lett. **109**, 146401 (2012).

⁷ H. Hadipour and Y. Yekta, Phys. Rev. B **100**, 195118 (2019).

⁸ Y. Yekta Kia, H. Hadipour, E. Sasoglu, C. Friedrich, S. A. Jafari, S. Blugel, and I. Mertig, Phys. Rev. Materials **5**, 030001 (2021).

⁹ Y. D. Wang, W. L. Yao, Z. M. Xin, T. T. Han, Z. G. Wang, L. Chen, C. Cai, Yuan Li, and Y. Zhang Nature Communications, **11**, 4215 (2020).

¹⁰ Eric B. Isaacs and Chris A. Marianetti, Phys. Rev. B **94**, 035120 (2016).

¹¹ M. A. McGuire, G. Clark, S. KC, W. M. Chance, G. E. Jellison, V. R. Cooper, X. Xu, and B. C. Sales, Phys. Rev. Materials **1**, 014001 (2017).

¹² Zh. Zhang, J. Shang, Ch. Jiang, A. Rasmita, W. Gao, and T. Yu, Nano Lett. **19**, 3138 (2019).

¹³ M. C. De Siena, S. E. Creutz, A. Regan, P. Malinowski, Q. Jiang, K. T. Kluherz, Gu. Zhu, Zh. Lin, J. J. De Yoreo, X. Xu, J. H. Chu, and D. R. Gamelin, Nano Lett. **20**, 2100 (2020).

¹⁴ K. L. Seyler, D. Zhong, D. R. Klein, Sh. Gao, X. Zhang, B. Huang, E. Navarro-Moratalla, L. Yang, D. H. Cobden, M. A. McGuire, W. Yao, D. Xiao, P. Jarillo-Herrero, and X. Xu, Nat. Phys. **14**, 277 (2018).

¹⁵ D. Shcherbakov, P. Stepanov, D. Weber, Y. Wang, J. Hu, Y. Zhu, K. Watanabe, T. Taniguchi, Zh. Mao, W. Windl, J. Goldberger, M. Bockrath, and Ch. N. Lau, Nano Lett. **18**, 4214 (2018).

¹⁶ Sh. Jiang, L. Li, Z. Wang, K. F. Mak, and J. Shan, Nat. Nanotechnol. **13**, 549 (2018).

¹⁷ S. Son, M. J. Coak, N. Lee, J. Kim, T. Y. Kim, H. Hamidov, H. Cho, Ch. Liu, D. M. Jarvis, Ph. A. C. Brown, J. H. Kim, Ch. H. Park, D. I. Khomskii, S. S. Saxena, and J. G. Park, Phys. Rev. B **99**, 041402(R) (2019).

¹⁸ T. Kong, K. Stolze, E. I. Timmons, J. Tao, D. Ni, S. Guo,

- Z. Yang, R. Prozorov, and R. J. Cava, *Adv. Mater. (Weinheim)* **31**, 1808074 (2019).
- 19 T. Kurumaji, S. Seki, S. Ishiwata, H. Murakawa, Y. Kaneko, and Y. Tokura, *Phys. Rev. B* **87**, 014429 (2013).
 - 20 O. Besbes, S. Nikolaev, N. Meskini, and I. Solovyev, *Phys. Rev. B* **99**, 104432 (2019).
 - 21 Sh. Tian, J. F. Zhang, Ch. Li, T. Ying, Sh. Li, X. Zhang, K. Liu, and H. Lei, *J. Am. Chem. Soc.* **141**, 5326 (2019).
 - 22 J. He, Sh. Ma, P. Lyua, and P. Nachtigall, *J. Mater. Chem. C* **4**, 2518 (2016).
 - 23 J. Liu, Q. Sun, Y. Kawazoed, and P. Jenac, *Phys. Chem. Chem. Phys.* **18**, 8777 (2016).
 - 24 D. Torelli, K. S. Thygesen, and T. Olsen, *2D Mater.* **6**, 045018 (2019).
 - 25 Y. Deng, Y. Yu, Y. Song, J. Zhang, N. Z. Wang, Z. Sun, Y. Yi, Y. Z. Wu, S. Wu, J. Zhu, J. Wang, X. H. Chen, and Y. Zhang, *Nature* **563**, 94 (2018).
 - 26 Z. Fei, B. Huang, P. Malinowski, W. Wang, T. Song, J. Sanchez, W. Yao, D. Xiao, X. Zhu, A. F. May, W. Wu, D. H. Cobden, J.-H. Chu, and X. Xu, *Nat. Mater.* **17**, 778 (2018).
 - 27 J. Li, B. Zhao, P. Chen, R. Wu, B. Li, Q. Xia, G. Guo, J. Luo, K. Zang, Z. Zhang, H. Ma, G. Sun, X. Duan, and X. Duan, *Adv. Mater.* **30**, 1801043 (2018).
 - 28 G. Duvjir, B. K. Choi, I. Jang, et al., *Nano Lett.* **18**, 5432 (2018).
 - 29 M. Bonilla, S. Kolekar, Y. Ma, H. C. Diaz, V. Kalappattil, R. Das, T. Eggers, H. R. Gutierrez, M. H. Phan, and M. Batzill, *Nat. Nanotechnol.* **13**, 289 (2018).
 - 30 Yuqiao Guo, Haitao Deng, Xu Sun, et al., *Adv. Mater.* **29**, 29, 1700715 (2017).
 - 31 Y. Ma, Y. Dai, M. Guo, C. Niu, Y. Zhu, and B. Huang, *ACS Nano* **6**, 1695 (2012).
 - 32 Xiong Wang, Dian Li, Zejun Li, Changzheng Wu, Chi-Ming Che, Gang Chen, and Xiaodong Cui, *ACS Nano* **15**, 10, 16236 (2021).
 - 33 K. Lasek, P. M. Coelho, K. Zborecki, et al., *ACS Nano* **14**, 8473 (2020).
 - 34 D. J. O'Hara, T. Zhu, A. H. Trout, A. S. Ahmed, Y. K. Luo, Ch. H. Lee, M. R. Brenner, S. Rajan, J. A. Gupta, D. W. McComb, and R. K. Kawakami, *Nano Lett.* **18**, 3125 (2018).
 - 35 Houlong L. Zhuang, Michelle D. Johannes, Michael N. Blonsky, and Richard G. Hennig, *Appl. Phys. Lett.* **104**, 022116 (2014).
 - 36 D. C. Freitas, R. Weht, A. Sulpice, G. Remenyi, P. Strobel, F. Gay, J. Marcus, and M. Nunez-Regueiro, *J. Phys. Condens. Matter* **27**, 176002 (2015).
 - 37 X. Sun, W. Li, X. Wang, Q. Sui, T. Zhang, Z. Wang, L. Liu, D. Li, S. Feng, S. Zhong, H. Wang, V. Bouchiat, M. Nunez Regueiro, N. Rougemaille, J. Coraux, A. Purbawati, A. Hadj-Azzem, Z. Wang, B. Dong, X. Wu, T. Yang, G. Yu, B. Wang, Z. Han, X. Han, and Z. Zhang, *Nano Research* **13**, 3358 (2020).
 - 38 A. Purbawati, J. Coraux, J. Vogel, A. Hadj-Azzem, N. Wu, N. Bendiab, D. Jegouso, J. Renard, L. Marty, V. Bouchiat, A. Sulpice, L. Aballe, M. Foerster, F. Genuzio, A. Locatelli, T. O. Montes, Z. V. Han, X. Sun, M. Nunez-Regueiro, and N. Rougemaille, *ACS Appl. Mater. Interfaces* **12**, 30702 (2020).
 - 39 Mohammad Rezwan Habib, Shengping Wang, Weijia Wang, Han Xiao, Sk Md Obaidulla, Anabil Gayen, Yahya Khan, Hongzheng Chen, and Mingsheng Xu, *Nanoscale* **11**, 20123 (2019).
 - 40 B. Li, Z. Wan, C. Wang, et al., *Nature Materials* **20**, 818 (2021).
 - 41 L. Meng, Z. Zhou, M. Xu, et al., *Nat Commun* **12**, 809 (2021).
 - 42 P. Chen, Y. -H. Chan, X. -Y. Fang, Y. Zhang, M. Y. Chou, S. -K. Mo, Z. Hussain, A. -V. Fedorov, and T. -C. Chiang, *Nature Communications* **6**, 8943 (2015).
 - 43 Katsuaki Sugawara, Yuki Nakata, Ryota Shimizu, Patrick Han, Taro Hitosugi, Takafumi Sato, and Takashi Takahashi, *ACS Nano* **10**, 1, 1341 (2016).
 - 44 J. Feng, D. Biswas, A. Rajan, et al., *Nano Lett.* **18**, 4493 (2018).
 - 45 P. Chen, W. W. Pai, Y. H. Chan, et al., *Phys. Rev. Lett.* **121**, 196402 (2018).
 - 46 A. O. Fumega, M. Gobbi, P. Dreher, W. Wan, C. Gonzalez-Orellana, M. Pena-Diaz, C. Rogero, J. Herrero-Martin, P. Gargiani, M. Ilyn, et al., *J. Phys. Chem. C* **123**, 27802 (2019).
 - 47 P. K. J. Wong, W. Zhang, F. Bussolotti, X. Yin, T. S. Herng, L. Zhang, Y. L. Huang, G. Vinai, S. Krishnamurthi, D. W. J. A. M. Bukhvalov, et al. *Adv. Mater.* **31**, 1901185 (2019).
 - 48 P. K. J. Wong, W. Zhang, F. Bussolotti, et al., *Adv. Mater.* **31**, 23 1901185 (2019).
 - 49 G. Vinai, C. Bigi, A. Rajan, et al, *Phys. Rev. B* **101**, 035404 (2020).
 - 50 R. Chua, J. Yang, X. He, et al., *Adv. Mater.* **32**, 202000693 (2020).
 - 51 W. Zhang, L. Zhang, P. K. J. Wong, et al, *ACS Nano*, **13**, 8997 (2019).
 - 52 O. V. Yazyev and L. Helm, *Phys. Rev. B* **75**, 125408 (2007).
 - 53 H. Hadipour, *Phys. Rev. B* **99**, 075102 (2019).
 - 54 E. Sasioglu, H. Hadipour, C. Friedrich, S. Blugel, and I. Mertig, *Phys. Rev. B* **95**, 060408(R) (2017).
 - 55 M. M. Ugeda, I. Brihuega, F. Guinea, and J. M. Gomez-Rodriguez, *Phys. Rev. Lett.* **104**, 096804 (2010).
 - 56 Z. Zhang, X. Zou, V. H. Crespi, and B. I. Yakobson, *ACS Nano* **7**, 10475 (2013).
 - 57 L. Cai, J. He, Q. Liu, et al., *J Am Chem Soc.* **137**, 2622 (2015).
 - 58 Wen-Yi Tong, Shi-Jing Gong, Xiangang Wan, and Chun-Gang Duan, *Nature Communications* **7**, 13612 (2016).
 - 59 L. Chengan, M. Yandong, Zh. Ting, X. Xilong, H. Baibiao, D. Ying, *New J. Phys.* **22** 033002 (2020).
 - 60 Huei-Ru Fuh, Ching-Ray Chang, Yin-Kuo Wang, Richard F. L. Evans, Roy W. Chantrell, and Horng-Tay Jeng, *Sci. Rep.* **6**, 32625 (2016).
 - 61 Kristian Sommer Thygesen, *2D Mater* **4**, 022004 (2017).
 - 62 Filip A. Rasmussen and Kristian S. Thygesen, *J. Phys. Chem. C* **119**, 13169 (2015)
 - 63 M. Cazzaniga, H. Cercellier, M. Holzmann, C. Monney, P. Aebi, G. Onida, and V. Olevano, *Phys. Rev. B* **85**, 195111 (2012).
 - 64 Marco Esters, Richard G. Hennig, and David C. Johnson, *Phys. Rev. B* **96**, 235147 (2017).
 - 65 Houlong L. Zhuang and Richard G. Hennig, *Phys. Rev. B* **93**, 054429 (2016).
 - 66 Cong Wang, Xieyu Zhou, Yuhao Pan, Jingsi Qiao, Xianguhua Kong, Chao-Cheng Kaun, and Wei Ji, *Phys. Rev. B* **97**, 245409 (2018).
 - 67 M. Cococcioni and S. de Gironcoli, *Phys. Rev. B* **71**, 035105, (2005).
 - 68 F. Aryasetiawan, M. Imada, A. Georges, G. Kotliar, S. Biermann, and A. I. Lichtenstein, *Phys. Rev. B* **70**, 195104

- (2004); F. Aryasetiawan, K. Karlsson, O. Jepsen, and U. Schönberger, *ibid.* **74**, 125106 (2006); T. Miyake, F. Aryasetiawan, and M. Imada, *ibid.* **80**, 155134 (2009).
- ⁶⁹ Y. Nomura, M. Kaltak, K. Nakamura, C. Taranto, S. Sakai, A. Toschi, R. Arita, K. Held, G. Kresse, and M. Imada, *Phys. Rev. B* **86**, 085117 (2012); B.-C. Shih, Y. Zhang, W. Zhang, and P. Zhang, *ibid.* **85**, 045132 (2012).
- ⁷⁰ G. Schönhoff, M. RoSner, E. Kamil, J. Berges, and T. Wehling, *APS March Meeting Abstracts*, **2018**, S35-007 (2018).
- ⁷¹ Angus Huang , Chin-Hsuan Chen , Ching-Hao Chang , and Horng-Tay Jeng, *Nanomaterials* **11**, 1998 (2021).
- ⁷² Li. Fengyu, Tu. Kaixiong, and Zhongfang Chen, *J. Phys. Chem. C* **118**, 21264 (2014).
- ⁷³ N. Marzari and D. Vanderbilt, *Phys. Rev. B* **56**, 12847 (1997).
- ⁷⁴ F. Freimuth, Y. Mokrousov, D. Wortmann, S. Heinze, and S. Blügel, *Phys. Rev. B* **78**, 035120 (2008).
- ⁷⁵ <http://www.flapw.de/MaX-5.0/>
- ⁷⁶ J. P. Perdew, K. Burke, and M. Ernzerhof, *Phys. Rev. Lett.* **77**, 3865 (1996).
- ⁷⁷ A. A. Mostofi, J. R. Yates, Y.-S. Lee, I. Souza, D. Vanderbilt, and N. Marzari, *Comput. Phys. Commun.* **178**, 685 (2008).
- ⁷⁸ C. Friedrich, S. Blügel, and A. Schindlmayr, *Phys. Rev. B.* **81**, 125102 (2010).
- ⁷⁹ G. Stollhoff, A. M. Oles, and V. Heine, *Phys. Rev. B* **41**, 7028 (1990).